Materials Today Bio 32 (2025) 101666

Contents lists available at ScienceDirect

Materials Today Bio

journal homepage: www.journals.elsevier.com/materials-today-bio

Ultrasound-actuated ion homeostasis perturbator for oxidative damage-augmented Ca^{2+} interference therapy and combined immunotherapy

Mi Yang, Yaqin Hu, Xiuxiu Hao, Qiaoqi Chen, Yang Cao, Haitao Ran *, Wei Zhang **

Department of Ultrasound, Second Affiliated Hospital of Chongqing Medical University. Chongqing, 400010, China

ARTICLE INFO

Keywords:
Ultrasound
Sonodynamic therapy
Reactive oxygen species
Immunogenic death

ABSTRACT

Calcium ion therapy has shown promise for cancer treatment, but its efficacy is limited by the cellular calcium buffering mechanism. Herein, an ion homeostasis disruptor (PCCa) was synthesized using an in situ mineralization method. The surface of the porphyrin-metal-organic framework PCN was coated with calcium carbonate ($CaCO_3$), aimed at causing Ca^{2+} overload and disrupting the self-defense mechanism during ion imbalance. Upon internalization into tumor cells, PCCa undergoes lysosomal acidification-induced $CaCO_3$ decomposition, leading to instantaneous Ca^{2+} overload. Simultaneously, under ultrasonic irradiation, the meso-tetra-(4-carboxyphenyl) porphine (TCPP) within the ion homeostasis disruptor generates reactive oxygen species (ROS), which impairs cellular calcium buffering capacity and amplifies cell damage caused by calcium overload. In addition, PCCa could also induce immunogenic cell death, release tumor-associated antigens (TAA), and act as an adjuvant, thereby promoting dendritic cell maturation and enhancing the antitumor activity of $CD8^+$ T cells. In mouse models, PCCa not only led to significant regression of subcutaneous mammary tumors but also demonstrated substantial anti-metastatic effects. In summary, the proposed ultrasound-actuated Ca^{2+} interference strategy is promising to deactivate the ion homeostasis maintenance system, contributing to the attainment of splendid tumor treatment outcome with reliable biosafety, which may provide useful insights in cancer therapy.

1. Introduction

Breast cancer is a prevalent malignancy affecting women that originates in the breast ducts, connective tissue, or lobules [1–3]. Although traditional tumor chemotherapy is widely used, its effectiveness is hindered by tumor complexity, unpredictability, and drug resistance [4,5]. Hence, there is an imminent necessity for efficacious and pragmatic therapeutic approaches to tackle the prevailing challenges in global breast cancer management. Cellular processes, guided by intricate regulatory mechanisms, can be targeted for cancer therapy [6,7]. Among these targets, calcium ions (Ca^{2+}) play essential roles as second messengers in cellular metabolism and information transmission [8,9]. Intracellular calcium overload disrupts cellular function, leading to mitochondrial dysfunction and heightened apoptotic signaling through oxidative stress [10–12]. This suggests that calcium overload could be used as a potential therapeutic strategy for cancer treatment. Moreover, it can induce immunogenic cell death, stimulate dendritic cell (DC) maturation, and activate the immune response [13–15]. Thus, inducing mitochondrial Ca^{2+} overload could be a promising approach to trigger apoptosis in tumor cells.

Recent advancements in cancer therapy involve nano-modulators tailored to exploit tumor microenvironmental responses, particularly those based on calcium phosphate and carbonate ($CaCO_3$) [16–18]. These modulators disrupt mitochondrial calcium homeostasis, inducing morphological abnormalities, membrane potential decline, and mitochondrial dysfunction. Calcium carbonate nanoparticles, known for their robust biocompatibility and biodegradability, enable precise Ca^{2+} delivery, making them ideal vectors for targeted Ca^{2+} release into tumor cells [19,20]. However, it is necessary to acknowledge that cells possess regulatory mechanisms, such as ion transporters [21,22], which actively

* Corresponding author. Department of Ultrasound, Second Affiliated Hospital of Chongqing Medical University. No. 74 Linjiang Rd, Yuzhong District, Chongqing, 400010, China.
** Corresponding author. Department of Ultrasound, Second Affiliated Hospital of Chongqing Medical University. No. 74 Linjiang Rd, Yuzhong District, Chongqing, 400010, China.
E-mail addresses: 300190@cqmu.edu.cn (H. Ran), 306902@hospital.cqmu.edu.cn (W. Zhang).

https://doi.org/10.1016/j.mtbio.2025.101666
Received 12 December 2024; Received in revised form 8 March 2025; Accepted 13 March 2025
Available online 13 March 2025

remove excess ions, thereby buffering intracellular calcium levels. These defense systems limit the efficacy of calcium ion therapy. To overcome this limitation, we combine calcium ion therapy with sonodynamic therapy (SDT). SDT is a widely used anticancer treatment that disrupts cancer cell oxidative balance by generating singlet oxygen via ultrasound (US), causing damage to organelles, particularly mitochondria and endoplasmic reticulum (ER), which then substantially reduces cellular calcium buffering capacity [19,23,24]. Thus, cells become more susceptible to calcium overload, which enhances the therapeutic potential of calcium ion therapy.

In this study, we developed an ultrasound-actuated calcium ion nano-modulator (PCCa) that efficiently induces apoptosis or directly kills tumor cells by SDT with mitochondrial calcium overload (Scheme 1). To achieve this, we coated PCN with a calcium carbonate layer and synthesized a mineralized porphyrin metal-organic framework. PCN, commonly used as a sound sensitizer in SDT [25,26], generates singlet oxygen efficiently under ultrasonic irradiation, thus enhancing cellular sensitivity to excess calcium ions and impairing cell activity. Additionally, calcium carbonate can degrade in an acidic environment, releasing calcium ions that lead to calcium overload, particularly within acidic lysosomes [27]. Upon PCCa endocytosis, ultrasonic irradiation triggers singlet oxygen production and shifts intracellular calcium concentrations, resulting in a synergistic amplification effect. Notably, both SDT and calcium overload can induce immunogenic cell death, suggesting that PCCa may enhance immunogenic death and initiate an antitumor immune response. Moreover, PCCa can be used as an immunological adjuvant to enhance the effectiveness of immunotherapy due to the auxiliary action of calcium carbonate. Therefore, PCCa can induce immunogenic cell death, promote adjuvant antigen presentation, stimulate the immune system, and facilitate comprehensive, long-term antitumor immunotherapy. When combined with an immune checkpoint inhibitor (αPD-1), PCCa activates immune effector cells and effectively suppresses tumor development. Overall, the mineralized porphyrin metal-organic framework nanosystem shows significant potential for improving tumor treatment efficiency, enhancing the immune system to inhibit tumor metastasis, and offering a promising strategy for breast cancer combination treatment.

2. Experimental section

2.1. Materials

Tetrakis(4-carboxyphenyl)porphyrin (TCPP) was purchased from Tokyo Chemical Industry CO., Ltd. Chloride octahydrate ($ZrOCl_2{\cdot}8H_2O$) and benzoic acid (BA) were bought from Adama-Beta Co., Ltd. Calcium chloride ($CaCl_2$) anhydrous and ammonium bicarbonate (NH_4HCO_3) were acquired from Aladdin (China). N,N′-dimethylformamide (DMF) was obtained from Adama-Beta Co., Ltd (China). 1,3-diphenylisobenzofuran (DPBF) was purchased from Sigma-Aldrich (USA). 2′,7′-Dichlorofluorescin diacetate (DCFH-DA), Calcein-AM, propidium iodide (PI), and Cell Counting Kit-8 were obtained from Dojindo (Japan). The Mitochondrial Membrane Potential (MMP) assay kit with JC-1 was sourced from Beijing Solarbio Science & Technology Co., Ltd. All cell culture-related reagents were procured from Beyotime Institute of Biotechnology (China).

2.2. Cell lines and animals

The mouse 4T1 cell line was purchased from the Chinese Academy of Sciences Shanghai Cell Bank (Shanghai, China) and cultured in RPMI-1640 medium supplemented with 10 % fetal bovine serum and 1 % penicillin-streptomycin. The cells were cultured in a CO2 incubator at 37 °C under a humidified atmosphere with 5 % carbon dioxide.

Female BALB/c mice (4–6 weeks old) were obtained from the Animal Center of Chongqing Medical University and housed under standard conditions. All animal experiments were conducted following approval

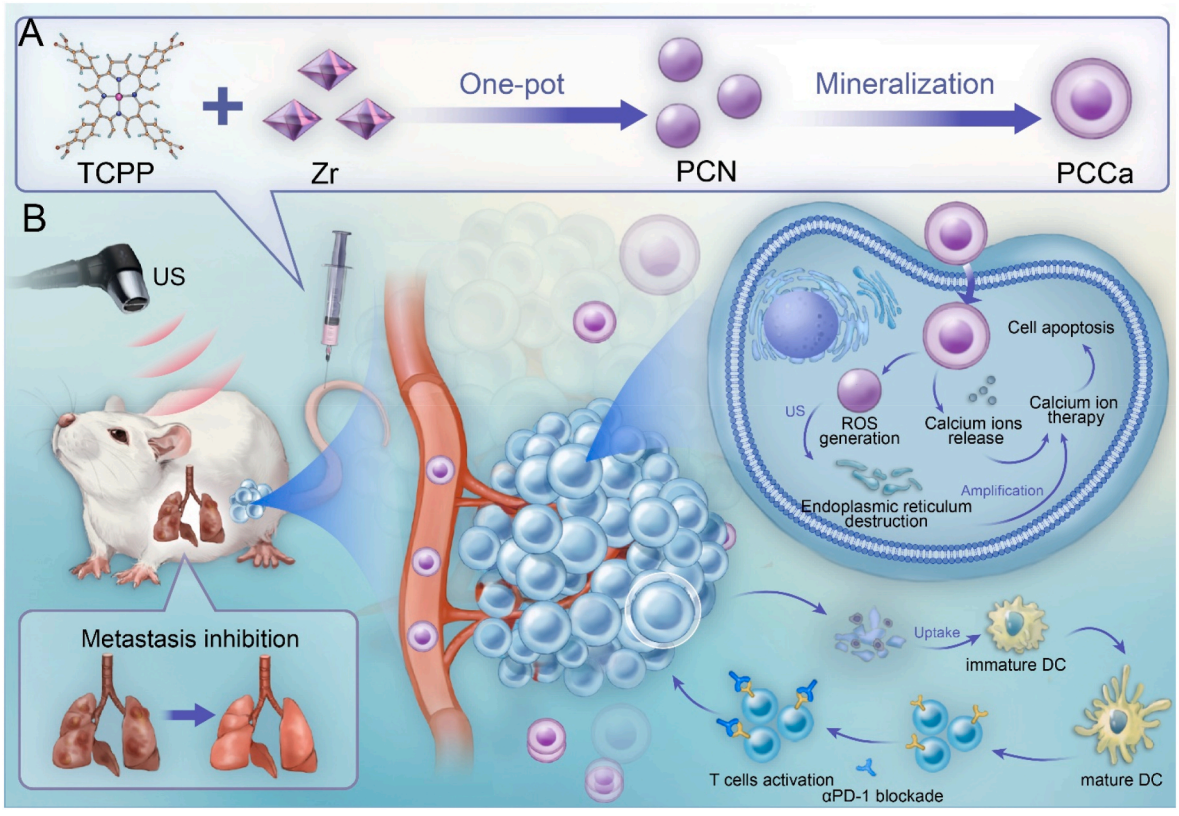

Scheme 1. Schematic illustration of a PCCa platform for ROS-mediated calcium ion therapy. (A) preparation of PCCa. (B) The tumor cell death process by calcium ion therapy and PCCa mediated cancer immunotherapy.

from the Animal Ethics Committee of Chongqing Medical University. To establish the tumor model, each BALB/c mouse received a subcutaneous injection of 1×10^6 4T1 cells into the right breast pad.

2.3. Preparation of nanoparticles

2.3.1. Synthesis of PCN

Herein, 100 mg of TCPP, 2800 mg of benzoic acid and 300 mg of $ZrOCl_2{\cdot}8H_2O$ were dissolved in 100 mL of DMF and stirred magnetically for 5 h at 90 °C. The precipitate was then centrifuged at 8000 g for 10 min and washed three times with DMF.

2.3.2. Synthesis of PCCa

Briefly, 16.61 mg of $CaCl_2$ was added to 50 mL of PCN solution (20 μg mL^{-1}) in ethanol at room temperature. Subsequently, the bottle was placed in a sealed container with another bottle containing 6000 mg of NH_4HCO_3, also at room temperature. After 12 h, the PCCa products were obtained by centrifugation at 8000 rpm for 10 min and washed three times with ethyl alcohol.

2.4. Characterization of nanoparticles

The morphologies of PCCa were examined using transmission electron microscopy (TEM) with a working voltage of 200 kV (JEM-2100, Japan). High-angle annular dark field (HAADF) scanning TEM (STEM) and energy-dispersive X-ray (EDX) analyses were conducted using a ThermoFisher Scientific Talos F200S field-emission TEM. The average particle size and zeta potential were determined using a Malvern Zetasizer Nano ZS90 analyzer at room temperature. UV–Vis absorption spectra were acquired using a UV–Vis spectrophotometry Lambda 950 (USA). Fourier transform infrared (FTIR) spectroscopy was performed using an FTIR5700 instrument (Thermo Scientific).

2.5. Ca^{2+} production by nanoparticles

4T1 cells were seeded in confocal dishes at a density of 1×10^5 cells per well and cultured for 24 h. Then, the cells were treated with a medium containing different nanoparticles (PBS, PCN, and PCCa, each at 100 μg mL^{-1}) for 4 h. For the US group, the cells were exposed to low-intensity focused ultrasound (LIFU) for 2 min at 1.5 W cm^{-2}. After treatment, the cells were washed three times and stained with a Fluo-3 AM calcium fluorescent probe, and calcium was observed using confocal laser scanning microscopy (CLSM, A1R; Nikon, Tokyo, Japan).

2.6. Cellular uptake of nanoparticles

4T1 cells were seeded in confocal dishes at a density of 1×10^5 cells per well and cultured overnight. The cells were then treated with free PCCa for various durations (1, 2, 3, and 4 h). After the treatment, the cells were washed three times with PBS, fixed with 4 % paraformaldehyde for 10 min, and the nuclei were stained with DAPI. Cellular uptake ability was evaluated using CLSM.

Additionally, 4T1 cells were seeded in a 12-well plate at a density of 1×10^5 cells per well and cultured overnight, following which the cells were treated with free PCCa for different durations (1, 2, 3, and 4 h). After treatment, the cells were washed three times with PBS and then collected, and the cellular uptake of nanoparticles was quantified using flow cytometry.

2.7. Detection of $^1O_2$

For the detection of $^1O_2$ using 1,3-diphenylisobenzofuran (DPBF), a total of 50 μL of DPBF solution (2 mg mL^{-1}), 50 μL of different nanoparticles (distilled water, PCN, and PCCa), and 400 μL of DMF were combined in an Eppendorf tube. The mixture was then exposed to US irradiation at 1.5 W cm^{-2} in the dark for various durations. The absorption spectra were recorded using a multimode reader.

For electron spin resonance (ESR) measurement, 20 μL of TEMP solution was mixed with 1 mL of PCCa dispersion (100 μg mL^{-1}). The mixture was then irradiated with US (1.5 W cm^{-2}) for different durations, and the signals were recorded using an ESR spectrometer.

2.8. In vitro ROS detection

4T1 cells were incubated with a medium containing different nanoparticles (PBS, PCN, and PCCa, each at 100 μg mL^{-1}) for 4 h. Next, the cells were washed with PBS three times, and 100 μL of DCFH-DA in serum medium (20 μM) was added. The cells were then divided into five groups: PBS, LIFU, PCCa, PCN + LIFU, and PCCa + LIFU. After irradiation with LIFU (1.5 W cm^{-2}, 2 min), the cells were washed, stained with DAPI for 10 min, washed with PBS and then imaged using CLSM.

Additionally, 4T1 cells were seeded in a 12-well plate at a density of 1×10^5 cells per well and cultured with a medium containing different nanoparticles (PBS, PCN, and PCCa, each at 100 μg mL^{-1}) for 4 h. The cells were then washed with PBS three times, and 100 μL of DCFH-DA in serum medium (20 μM) was added. Similar to the previous procedure, the cells were divided into five groups: PBS, LIFU, PCCa, PCN + LIFU, and PCCa + LIFU. After LIFU irradiation (1.5 W cm^{-2}, 2 min), the cells were washed and collected, and the fluorescence intensity of each group was determined using flow cytometry.

2.9. Cytotoxicity evaluation

The cytotoxicity of the PCCa was assessed using a standard CCK-8 assay. Firstly, human umbilical vein endothelial cells (HUVECs) were seeded onto 96-well plates at a density of 5×10^3 cells per well. After 24 h of incubation, the medium was replaced with different concentrations (0, 10, 25, 50, 100, 200 μg mL^{-1}) of PCCa aqueous solutions and incubated for 24 h and 48 h. The cell viability was estimated using the CCK-8 assay following the manufacturer's protocol.

Then, the therapeutic efficacy of various treatments was evaluated *in vitro*. 4T1 cells were seeded onto 96-well plates at a density of 5×10^3 cells per well and cultured for 24 h. The medium was then replaced with different solutions at various concentrations and incubated at 37 °C with 5 % CO_2. The different treatment groups included PBS, LIFU, PCN, PCCa, PCN + LIFU, and PCCa + LIFU. For the LIFU group, cells were irradiated with LIFU (1.5 W cm^{-2}) for 2 min. The cell viability of each group was assessed using the CCK-8 assay.

2.10. Live/dead cell staining assay

To further assess the synergistic effect of therapy on cancer cells, 4T1 cells were seeded in confocal dishes at a density of 1×10^5 cells per well and cultured for 24 h. Then, the cells were divided into five groups: free RPMI-1640, LIFU, PCN, PCCa, PCN + LIFU, and PCCa + LIFU. For the LIFU group, the cells were irradiated with LIFU (1.5 W cm^{-2}) for 2 min. After treatment with different regimens, the cells were incubated with Calcein-AM (15 μL) and propidium iodide (PI) (5 μL) for 15 min. Lastly, the cells were washed with PBS three times and visualized using CLSM.

2.11. Cell apoptosis assay

4T1 cells were seeded in a 12-well plate at a density of 1×10^5 cells per well and cultured for 24 h, following which they were divided into five groups: free RPMI-1640, LIFU, PCN, PCCa, PCN + LIFU, and PCCa + LIFU. For the LIFU group, the cells were irradiated with LIFU (1.5 W cm^{-2}) for 2 min. After treatment with different regimens, the cells were washed, collected, and then incubated with V-FITC/PI for 20 min. Their apoptosis rates were calculated by flow cytometry (Cytomic FC 500 MCL, Beckman, USA).

2.12. Detection of MMP

4T1 cells were seeded in confocal dishes at a density of 1×10^5 cells per well and cultured for 24 h. Then, the cells were cultured with a medium containing different nanoparticles (PBS, PCN, and PCCa, each at 100 μg mL^{-1}) for 4 h and divided into five groups: PBS, LIFU, PCCa, PCN + LIFU, and PCCa + LIFU. For the LIFU group, the cells were irradiated with LIFU (1.5 W cm^{-2}) for 2 min. After culturing for an additional 2 h, the cells were stained with JC-1 (5 μg mL^{-1}) for 30 min and washed three times, and the variation in mitochondrial membrane potential (MMP) was observed using CLSM.

2.13. DAMPs release and DCs activation in vitro

To evaluate immunogenic cell death (ICD) biomarkers, namely calreticulin (CRT), High Mobility Group Box-1 (HMGB1), and Adenosine triphosphate (ATP), 4T1 cells were seeded in a 6-well plate and subjected to treatment procedures similar to those in the JC-1 MMP detection assay. Then, the cells were stained with anti-CRT antibody (FITC conjugated) and analyzed using flow cytometry. The culture supernatant was collected to measure the concentrations of HMGB1 and ATP using enzyme-linked immunosorbent assay (ELISA).

To investigate the *in vitro* maturation of DCs induced by different treatments, 4T1 cells were seeded into the upper chamber of transwell devices, while bone marrow-derived DCs (BMDCs) from mouse bone marrow were plated into the bottom chamber. Then, the 4T1 cells were cultured with a medium containing different nanoparticles (PBS, PCN, and PCCa, each at 100 μg mL^{-1}) and divided into five groups: PBS, LIFU, PCCa, PCN + LIFU, and PCCa + LIFU. After 4 h of nanodrug incubation, all groups subjected to US treatment were irradiated with LIFU (1.5 W cm^{-2}) for 2 min. The BMDCs were then cultured for an additional 24 h, and collected for flow cytometry analysis to detect mature DCs ($CD11c^+$ $CD80^+$ $CD86^+$).

2.14. In vivo biodistribution and biosafety assays

To investigate the biodistribution of PCCa in tumor-bearing mice, near-infrared fluorescent dyes (DIR) were loaded into PCCa and intravenously injected into the mice. Tumor-bearing mice were injected 200 μL of DIR-labeled PCCa nanoparticles (10 mg kg^{-1}) through the tail vein. *In vivo* imaging was conducted at various intervals post-injection using an *in vivo* imaging system, following which the tumors and major organs were harvested for *ex vivo* imaging, and the corresponding fluorescence intensities were measured.

Blood biochemical markers and standard blood examinations were conducted to assess the biosafety of PCCa. The mice were intravenously injected with PCCa and sacrificed at predetermined time points to collect biological samples for analysis.

2.15. In vivo antitumor efficiency

For *in vivo* synergistic therapy, mice bearing 4T1 tumors were randomly assigned to seven groups (n = 8 per group): (1) Control, (2) LIFU, (3) PCCa, (4) PCCa + α-PD-1, (5) PCN + LIFU, (6) PCCa + LIFU, and (7) PCCa + LIFU + α-PD-1. Tumor-bearing mice received intravenous injections of PCCa saline solution (200 μL, 20 mg kg^{-1}) for Groups 3, 4, 6 and 7, or PCN-224 saline solution (200 μL, 20 mg kg^{-1}) for Group 5. At 24 h post-injection, mice in Groups 2, 5, 6 and 7 had their tumor areas exposed to LIFU (1.5 W cm^{-2}, 10 min). For Groups 4 and 7, the mice were intraperitoneally injected with α-PD-1 (100 μg per mouse) on days 2, 4 and 6.

For the lung metastasis tumor model, approximately 1×10^5 cells were intravenously injected into mice on day 8. Tumor volumes (length × $width^2/2$) and mouse weights were recorded every two days. The mice were euthanized when their tumor volumes reached 2500 mm^3. On day 14, three mice from each group were sacrificed to harvest the tumors, major organs, and peripheral blood. DCs in tumor tissues were analyzed using flow cytometry. Tumor-infiltrating $CD8^+$ T cells were labeled with flow antibodies (anti-CD3, anti-CD4, and anti-CD8 antibodies) after digestion with digestive enzymes and analyzed by flow cytometry. Tumor necrosis factor-alpha (TNF-α) and interferon-gamma (IFN-γ) levels were detected by ELISA.

At the end of treatment, all mice were sacrificed, and metastatic tumor lesions in the lungs were counted. Tumor tissues were detached for TUNEL, PCNA, and H&E staining analysis, while the lungs were used for H&E staining analysis.

2.16. Statistical analysis

The data are shown as mean ± standard deviation (SD). For comparisons between two groups, *t*-test was performed, and for comparisons between three or more independent groups, one-way analysis of variance (ANOVA) was conducted. Statistical analysis was conducted using GraphPad Prism 6, and $P < 0.05$ was considered statistically significant.

3. Results and discussion

3.1. Fabrication and characterization of PCCa

In this study, PCN was selected as the nanocarrier due to its adjustable exterior surface properties and remarkable ability to generate reactive oxygen species upon ultrasonic irradiation [28,29]. The size and shape of PCN were modified by adding molecules (such as benzoic acid). Given the well-established evidence indicating the acidic microenvironment differences between tumors and normal tissues, an acidic decomposable $CaCO_3$ shell was chosen. The PCN was then coated with a $CaCO_3$ mineralized layer using a seed growth strategy to obtain the nanoplatform PCCa. As shown in Scheme 1, the metal-organic framework PCN was first prepared, followed by coating the $CaCO_3$ shell through in situ mineralization to obtain PCCa.

PCN was constructed following a previously reported method [30]. TEM and SEM images revealed a uniform morphology with diameters of approximately 100 nm (Fig. 1a). Then, PCN was coated with a $CaCO_3$ mineralized layer, and the successful coating of the $CaCO_3$ mineralized layer around PCN was confirmed by TEM and SEM images. While the overall morphology remained similar, there was a noticeable increase in nanoparticle size, indicating the adoption of the PCN structure by PCCa. The composition of PCCa was further characterized by TEM and EDX elemental mapping images. Zr was scattered in the core, and Ca was primarily distributed in the mineralized shell, as Fig. 1b illustrates. High-intensity signals were seen at the distinctive peaks of Zr and Ca in the EDX spectrum (Fig. S1). We have conducted Brunauer Emmett Teller (BET) analysis to further illustrate the changes in specific surface area before and after modification. The specific surface area decreased from 523.8593 m^2/g (before modification) to 96.0127 m^2/g (after modification). The results show a significant decrease in the specific surface area post-modification, indicating successful coating of $CaCO_3$ (Fig. S2). The successful coating of $CaCO_3$ was also confirmed by XRD and XPS patterns (Figs. S3 and S4). The measured sizes by dynamic light scattering (DLS) were consistent with the TEM images (Fig. 1c).

Next, PCN and PCCa were analyzed using UV–vis absorbance spectroscopy. As shown in Fig. 1d, PCN and PCCa exhibited similar absorption spectra, indicating the successful coating of the $CaCO_3$ mineralized layer around PCN. The FTIR spectra of PCN, $CaCO_3$, and PCCa are shown in Fig. S5. The spectrum of PCCa displayed characteristic absorption bands of both PCN and $CaCO_3$, confirming the effective assembly of the final product. Zeta potentials of PCN, PCCa, $CaCO_3$ and were measured to be 14.6 and −25.1 mV, −29.1 mV, respectively (Fig. 1e). The significantly decreased zeta potential of PCCa may result from the negative potential of the $CaCO_3$ coating. Stability experiments demonstrated that PCN and PCCa remained stable in different simulated media at pH 7.4 (Fig. S6). Additionally, the pH-triggered degradation

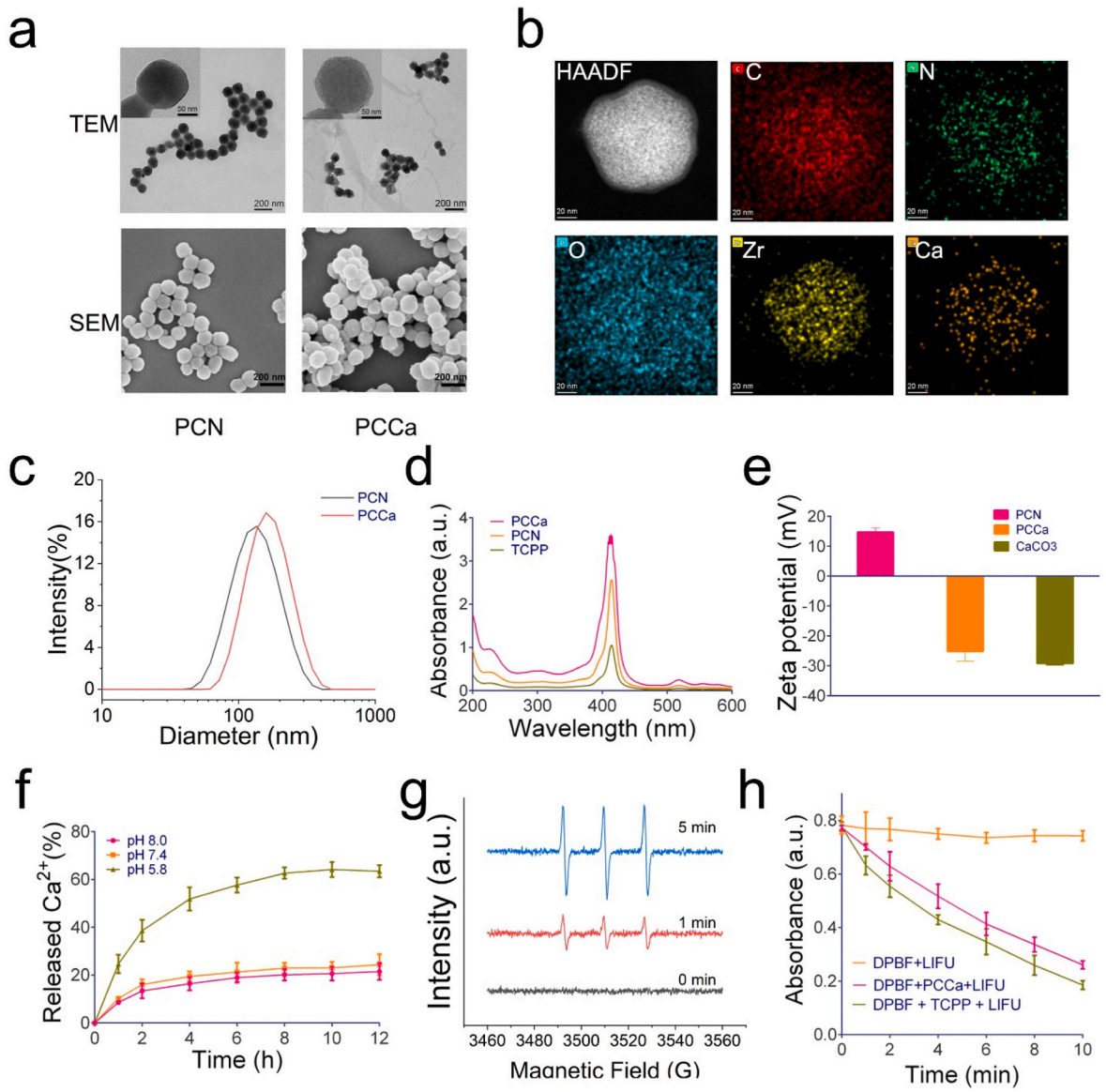

Fig. 1. Characterization of nanoparticles. (a) TEM and SEM images illustrating the morphology of PCN and PCCa. (b) Elemental mapping of PCCa showing the distribution of constituent elements. (c) Size distribution analysis of PCN and PCCa nanoparticles. (d) UV–vis absorption spectra of TCPP, PCN, and PCCa. (e) Zeta potential measurements of PCN, PCCa and, $CaCO_3$ (n = 3). (f) Quantification of Ca^{2+} release at different pH levels (n = 3). (g) ESR spectra illustrating the production of $^1O_2$. (h) Degradation of DPBF in the presence of TCPP or PCCa upon LIFU irradiation.

behavior of PCCa was evaluated in PBS with pH values of 5.8 and 7.4. As illustrated in Fig. S7, the morphology of the nanoplatform remained intact at pH 7.4, while the shell and core of PCCa degraded at pH 5.8 within 60 min.

The calcium ion release from PCCa in various pH solutions was quantified using ICP-MS. As shown in Fig. 1f, PCCa exhibited high efficiency in releasing calcium ions at pH 5.8. Analysis by ICP-MS revealed that the calcium fraction accounted for 18.6 % of PCCa. We speculated when PCCa was endocytosed in the tumor cells, its pH-responsive decomposition properties facilitated accelerated disintegration, leading to the release of more Ca^{2+} ions within the acidic microenvironment of the tumor, which then overloaded the mitochondria.

Our study, along with others, has demonstrated that PCN exhibits an excellent ability to elevate cellular oxidative levels and disrupt cell function [30–32]. Therefore, we initially investigated the singlet oxygen production efficiency of PCCa using electron spin resonance (ESR) spectroscopy, with TEMP as the spin trap for short-lived $^1O_2$ [33]. As shown in Fig. 1g, a significantly enhanced 1:1:1 $^1O_2$ signal was observed upon irradiating the mixture of TEMP and PCCa with LIFU (1.5 W cm^{-2}, 5 min), indicating the production of $^1O_2$ by PCCa following irradiation. Next, we used the DPBF colorimetric indicator to probe $^1O_2$ alternatively (Fig. 1h) and observed that ROS generation did not occur in the absence of PCCa. However, the decrease in absorbance of DPBF at 417 nm in the presence of PCCa was closely associated with the duration of LIFU irradiation, suggesting a controllable US-triggered $^1O_2$ production.

3.2. Cellular uptake and cellular calcium ion concentration in vitro

Based on the favorable fluorescence properties of PCCa, we investigated its cellular uptake by tracking the fluorescence signal using CLSM. As shown in Fig. S8, after 4h of co-incubation, the red fluorescence intensity in the cytoplasmic region increased with the extension of incubation time, indicating that the endocytosis of PCCa was time-dependent. Moreover, the results of quantitative analysis of intracellular fluorescence showed that the proportion of 4T1 cells that internalized a significant amount of PCCa reached as high as 88.36 % after 4

h of treatment (Fig. 2a). This rapid cellular uptake suggests the potential for highly effective tumor therapy. Bio-TEM images further confirmed the efficient endocytosis of nanoplatforms into the cells (Fig. 2b).

Nanoparticles typically enter cells via endocytosis [34]. Upon endocytosis into lysosomes, the $CaCO_3$ coating of PCCa degrades under low pH conditions, releasing calcium ions for cancer therapy. Initially, we confirmed that PCCa could indeed release calcium ions after being internalized into cells (Fig. 2c). Fluo-3 AM, a commonly used fluorescent probe for detecting intracellular calcium ion concentrations, was used for this purpose. When 4T1 cells treated with PCCa were stained with Fluo-3 AM, as depicted in and Figs. S9 and S10, the cells exhibited increased fluorescence intensity, indicating a higher quantity of calcium ions in the PCCa-treated group.

3.3. Detection of ROS in vitro

Intracellular ROS generation was assessed using the fluorescent probe 2′,7′-dichlorofluorescein diacetate (DCFH-DA) [35]. As shown in Fig. 3b, minimal fluorescence was observed in the control or free laser groups. Comparatively, PCN and PCCa nanomaterials containing TCPP showed intense green fluorescence under LIFU irradiation, indicative of increased ROS production (Fig. S11). Flow cytometry results revealed the highest fluorescence intensity in the PCCa + LIFU group, indicating the generation of substantial ROS (Fig. S12), consistent with the CLSM findings. These results demonstrate that PCCa can generate large quantities of ROS upon LIFU irradiation, thereby exacerbating cytotoxicity.

3.4. Cytotoxicity

Requisite biocompatibility is crucial to ensure the effective utilization of a material for its therapeutic functions, while minimizing any potential toxic or deleterious impact on normal tissues and organs [36]. To evaluate the cytotoxic effect of PCCa on HUVECs and 4T1 cells, a CCK-8 assay was conducted. As shown in Fig. 3a and Fig. S13, even after being treated with PCCa at a concentration of up to 200 μg mL^{-1} for 48 h, the mean survival rate of the cells was not less than 80 %, indicating that PCCa had good biocompatibility with cells.

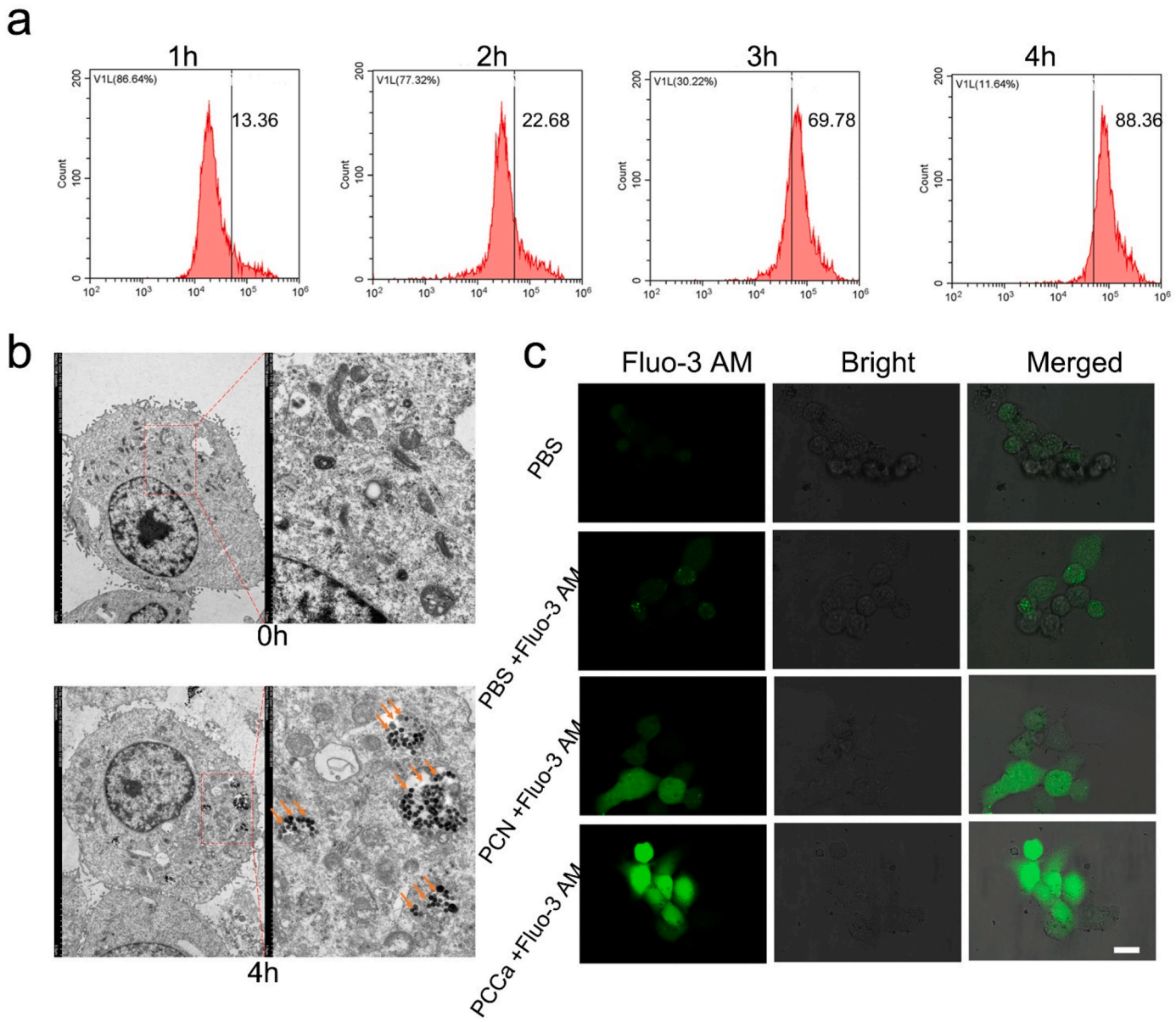

Fig. 2. (a) Quantification of nanoparticle cellular uptake by 4T1 cells using flow cytometry. (b) Visualization of nanoparticle internalization by 4T1 cells via TEM. (c) Observation of Ca^{2+} release from PCCa using CLSM (scale bar = 50 μm).

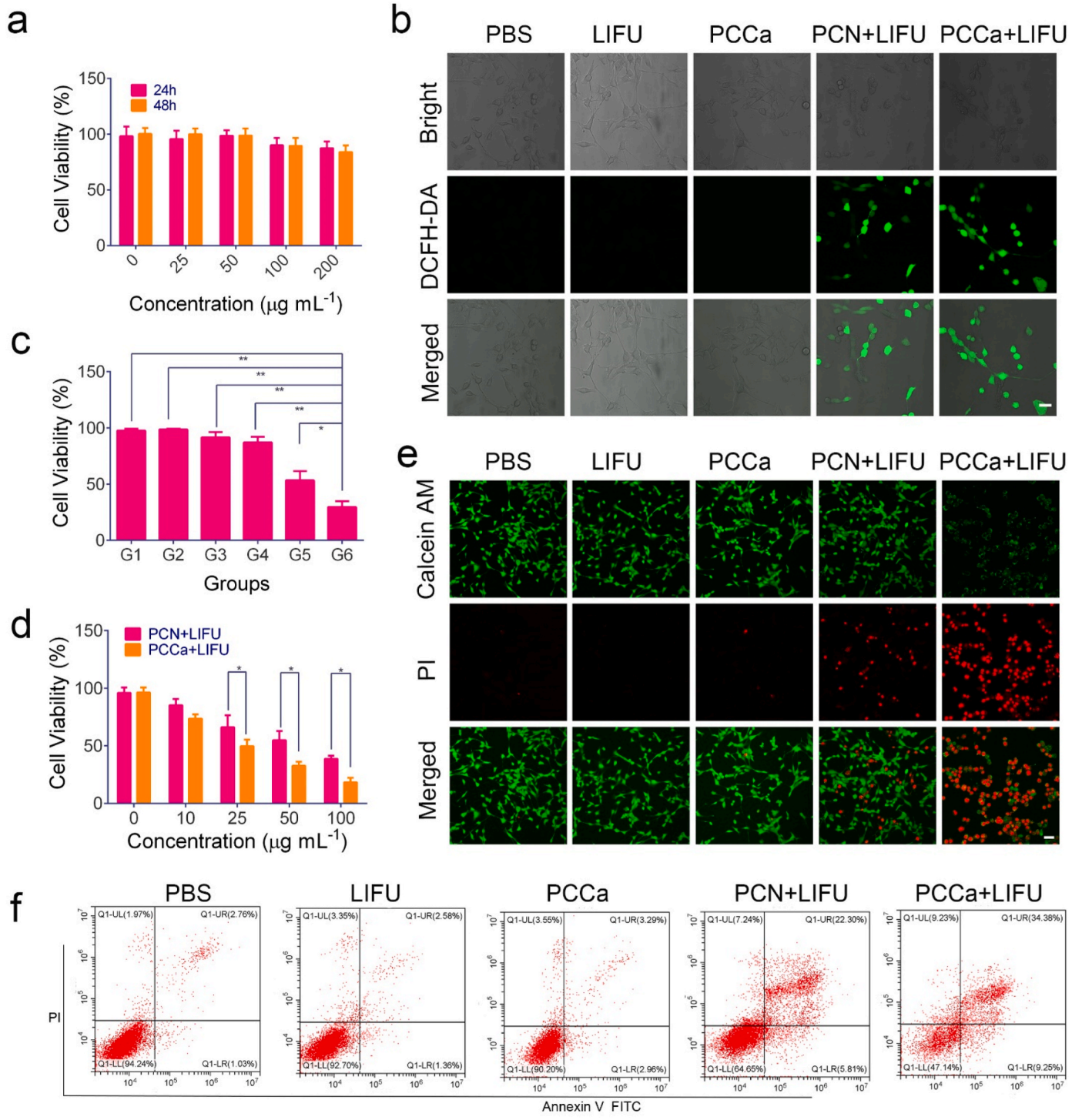

Fig. 3. (a) Assessment of PCCa cytotoxicity against HUVECs. (b) Evaluation of intracellular ROS generation post-irradiation using the ROS detection probe, DCFH-DA. Scale bar = 50 μm. (c) Viability of 4T1 cells post-treatment with different interventions (G1: PBS, G2: LIFU, G3: PCN, G4: PCCa, G5: PCN + LIFU, G6: PCCa + LIFU; n = 5). (d) Cytotoxicity evaluation of PCN and PCCa following LIFU irradiation (n = 5). (e) CLSM images of Calcein-AM/PI co-stained 4T1 cells after different treatments (scale bar = 50 μm). Red and green dots stand for dead and living cells, respectively. (f) Apoptotic analysis of 4T1 cells stained with Annexin V-FITC apoptosis detection kit after receiving various interventions. Statistical significance was assessed using one-way ANOVA. *$p < 0.05$, **$p < 0.01$.

Next, we assessed the *in vitro* cytotoxicity induced by nanoparticle treatment using a CCK-8 assay. The cell viability was detected under different ultrasound power and different irradiation time while other conditions were kept unchanged (Fig. S14). The results showed that cell viability decreased with increasing ultrasonic power and irradiation time. Finally, the following parameters were chosen: an ultrasound power of 2 Wcm^{-2} and an irradiation time of 120 s for the subsequent determination of cell viability. The tumor cells were found to be more sensitive to intracellular Ca^{2+} overload compared to healthy cells, as fluctuations in calcium levels can induce detrimental metabolic stress in carcinoma cells [37]. As shown in Fig. 3c, single treatments with LIFU irradiation or PCCa administration minimally affected tumor cell growth. Similarly, moderate tumor inhibition was observed with SDT treatment alone (PCN + LIFU group). In contrast, the PCCa + LIFU

group induced the most significant cell death, with cell viability decreasing to less than 50 %. The released Ca^{2+} from nanoparticles likely contribute to exacerbating intracellular Ca^{2+} dyshomeostasis by deactivating ion channels, thereby restraining cell proliferation and inducing apoptosis [38]. Thus, it can be deduced that SDT induced by PCN may synergize with Ca^{2+} overload to induce the highest degree of tumor cell destruction. Furthermore, the therapeutic efficacy of PCCa against tumor cells exhibited a typical dose-dependent response (Fig. 3d).

Moreover, the cell cytotoxicity of PCCa nanoparticles was examined using a live/dead cell staining assay (Fig. 3e). In this assay, red fluorescence PI and green fluorescence Calcein AM were utilized as dyes.

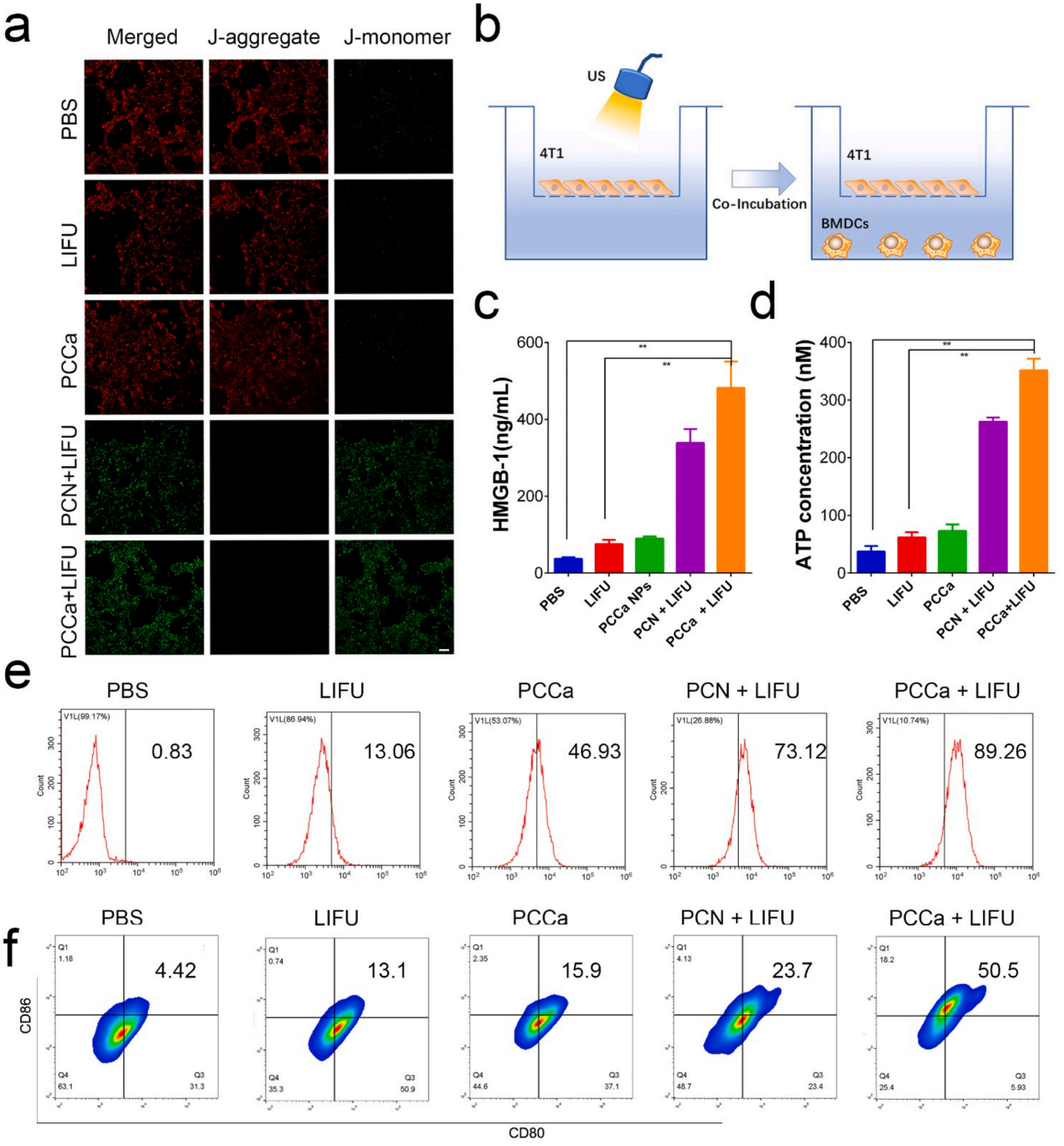

Fig. 4. (a) Confocal laser scanning microscopy (CLSM) images of 4T1 cells treated with various regimens and stained with JC-1 (scale bar = 50 μm). Red and green fluorescence indicate J-aggregate and J-monomer, respectively. (b) Schematic representation of the experimental setup for dendritic cells (DCs) maturation *in vitro*. (c) Secretion of HMGB-1 and (d) ATP in the co-culture system after different treatments (n = 3). (e) Detection of calreticulin (CRT) exposure on the cell surface of 4T1 cells using flow cytometry after diverse treatments. (f) Flow cytometric analysis of matured DCs ($CD80^+$ $CD86^+$) following incubation with 4T1 cells subjected to different treatments. Statistical significance was assessed using one-way ANOVA. *$p < 0.05$, **$p < 0.01$.

The results revealed a strong green signal in the PBS group, indicating minimal cellular death. In contrast, the PCCa + LIFU group exhibited a prominent red signal, indicating that the combined effect had the most significant *in vitro* cell cytotoxicity, consistent with the findings of the CCK8 assay. These results suggested that PCCa effectively induced cell death in most tumor cells through Ca^{2+} overload and SDT effects. Flow cytometry analysis was also conducted to assess the cell cytotoxicity induced by PCCa under LIFU irradiation. As shown in Fig. 3f, the apoptotic rates in the PCN + LIFU group and PCCa + LIFU group were 29.5 % and 43.5 %, respectively. Moreover, the apoptotic rate in the control group was negligible. CLSM images and flow cytometry results demonstrated that 4T1 cells treated with PCCa and LIFU irradiation exhibited the highest oxidative levels, indicating that the combination of SDT and calcium ion therapy might offer a more effective synergistic treatment.

3.5. Mitochondrial dysfunction induced by PCCa-mediated calcium overload and SDT

SDT-induced oxidative stress and cytosolic Ca^{2+} excess can impair mitochondrial respiratory chain function, resulting in MMP depolarization [39]. To better understand the apoptotic mechanism by which PCCa disrupts mitochondrial homeostasis, we employed the JC-1 MMP detection kit to analyze the effect of Ca^{2+} and LIFU irradiation on 4T1 cell mitochondria. The results showed that when MMP was high, JC-1 accumulated in the mitochondrial matrix, forming a polymer that emits red fluorescence [40]. In contrast, at lower membrane potentials, JC-1 exists as a monomer and emits green fluorescence. As shown in Fig. 4a, the cells exhibited red fluorescence when treated with LIFU alone. However, upon treatment with PCCa, the cells displayed increased green fluorescence, especially in combination with $CaCO_3$. Moreover, under LIFU irradiation, both PCN and PCCa groups exhibited a significantly elevated JC-1 monomer/aggregation ratio, with the PCCa group showing the highest ratio, indicating severe mitochondrial damage (Fig. S15). These findings suggest that the combined effects of $CaCO_3$ and LIFU substantially diminish MMP, disrupt mitochondrial homeostasis, and induce apoptosis.

3.6. DAMPs release and DCs activation in vitro

PCCa enhances cytotoxicity by synergizing calcium overload with SDT. Given that both SDT and calcium overload can induce immunogenic cell death (ICD), PCCa may similarly trigger ICD and release tumor-associated antigens, thereby eliciting a robust immunological response. DAMPs generated during ICD can engage pattern recognition receptors (PRRs) on DCs, thereby initiating diverse innate and adaptive immune responses [41]. *In vitro* DC maturation, a pivotal step in immune response cascades, was assessed using transwell devices (Fig. 4b). HMGB1 protein, a nuclear non-histone protein, can be secreted from the nucleus to the extracellular milieu in response to cell injury, activating innate immunity by enhancing neutrophil recruitment and macrophage production of proinflammatory cytokines [42]. In contrast to the predominant localization of HMGB1 in the nucleus area of untreated cells, 'PCCa + LIFU' resulted in significant leakage into the cytosolic space, which can be explained by a severe rupture of the nucleus envelop and plasma membrane (Fig. 4c). ATP is released from damaged cells to promote P2Y2R-mediated phagocytosis clearance and P2x7R-mediated activation of NLRP3 inflammasome [33,43]. This process is essential for recruiting DCs and inflammatory cells, and promoting the maturation of cytotoxic $CD8^+$ T cells. As anticipated, the 'PCCa + LIFU' treatment resulted in the most pronounced release of cytosolic ATP into the extracellular matrix, indicative of extensive tumor cell disruption (Fig. 4d). One hallmark of DAMP production from dying tumor cells is the pre-apoptotic translocation of intracellular calreticulin from the endoplasmic reticulum lumen to the plasma membrane surface [44]. A significant increase in intracellular CRT levels following treatment with PCCa + LIFU was observed (Fig. 4e), suggesting ER stress-induced CRT translocation. Changes in immunogenic markers (HMGB1, ATP, and CRT) indicate that PCCa + LIFU may induce greater immunogenic cell death. Additionally, PCCa's immunostimulatory effect was evaluated *in vitro*. After treatment with PBS, LIFU, PCCa, PCN + LIFU, or PCCa + LIFU, BMDCs were co-cultured with lytic cells, and the percentage of mature cells in each group was assessed using flow cytometry. As shown in Fig. 4f, the PCCa group exhibited a slightly higher BMDC maturation rate compared to the PBS group, suggesting that PCCa could induce modest BMDC maturation. Notably, PCCa + LIFU significantly enhanced BMDC maturation, indicating PCCa's ability to augment the anticancer immune response.

3.7. In vivo fluorescence imaging and tumor-specific biodistribution analysis

Considering that efficient accumulation of Ca^{2+} nano-modulators at the tumor site is essential for therapeutic effect, the biodistribution of PCCa was assessed to confirm the tumor-specific drug enrichment using *in vivo* fluorescence imaging (Fig. S16). The fluorescence signal in the tumor region was initially detected and intensified from 6 h post-injection. The strongest signal was observed at 24 h post-injection, indicating the successful enrichment of PCCa at the tumor site. By 48 h post-injection, the fluorescence signal had diminished, suggesting the clearance of nanoparticles from the body. Additionally, at 24 and 48 h after injection, the amount of PCCa in the tumor and main organs was assessed semi-quantitatively. Due to its prolonged circulation half-life and enhanced permeability and retention (EPR) impact, PCCa accumulated to its maximum in the tumor area at 24 h.

3.8. Biocompatibility assessment of PCCa nanoparticles based on blood markers and tissue histology

Blood biochemical markers and standard blood examination were conducted to evaluate the nanoparticles' biosafety. Briefly, the mice were intravenously injected with PCCa and sacrificed at predetermined time points to collect biological samples for analysis. The relevant indexes were assessed, and the results indicated that the main parameters in the biochemical assay and hematology analysis were within the normal range (Fig. S17), similar to those in the control group, suggesting that PCCa exhibited good biocompatibility. Hematoxylin and Eosin (H&E) staining was performed on the lung, liver, heart, kidney, and spleen to assess the tissue structure. After the injection period, the H&E staining images (Fig. S18) did not reveal any evident abnormalities in these organs. Thus, PCCa also demonstrated good biocompatibility.

3.9. Tumor elimination efficiency of PCCa

We assessed the anticancer effects of PCCa *in vivo* based on the encouraging evidence of effectiveness and immune activation induced by ICD *in vitro*. As shown in Fig. 5a, the anticancer efficacy of PCCa was investigated in a 4T1 tumor-bearing BALB/c mouse model. The tumor-bearing mice were randomly assigned to seven groups (Control, LIFU, PCCa, PCCa + α-PD-1, PCN + LIFU, PCCa + LIFU, PCCa + LIFU + α-PD-1) and administered intravenous injections of nanoparticles. As shown in Fig. 5b, the PCN + LIFU, PCCa + LIFU, and PCCa + LIFU + α-PD-1 groups exhibited a significant reduction in tumor volume compared to the Control group, whereas the tumor volume in the PBS group increased 8-fold during treatment. Tumor weight measurements (Fig. 5c) and images of tumor tissue (Fig. 5d) further illustrated the therapeutic outcome. To assess treatment effects from a microscopic perspective, the tumor samples were stained using H&E, terminal deoxynucleotidyl transferase dUTP nick end labeling (TUNEL), and proliferating cell nuclear antigen (PCNA). As shown in Fig. 5e–H&E staining and immunohistochemical staining assay images revealed a large tumor cell population in the PBS group with evident proliferation

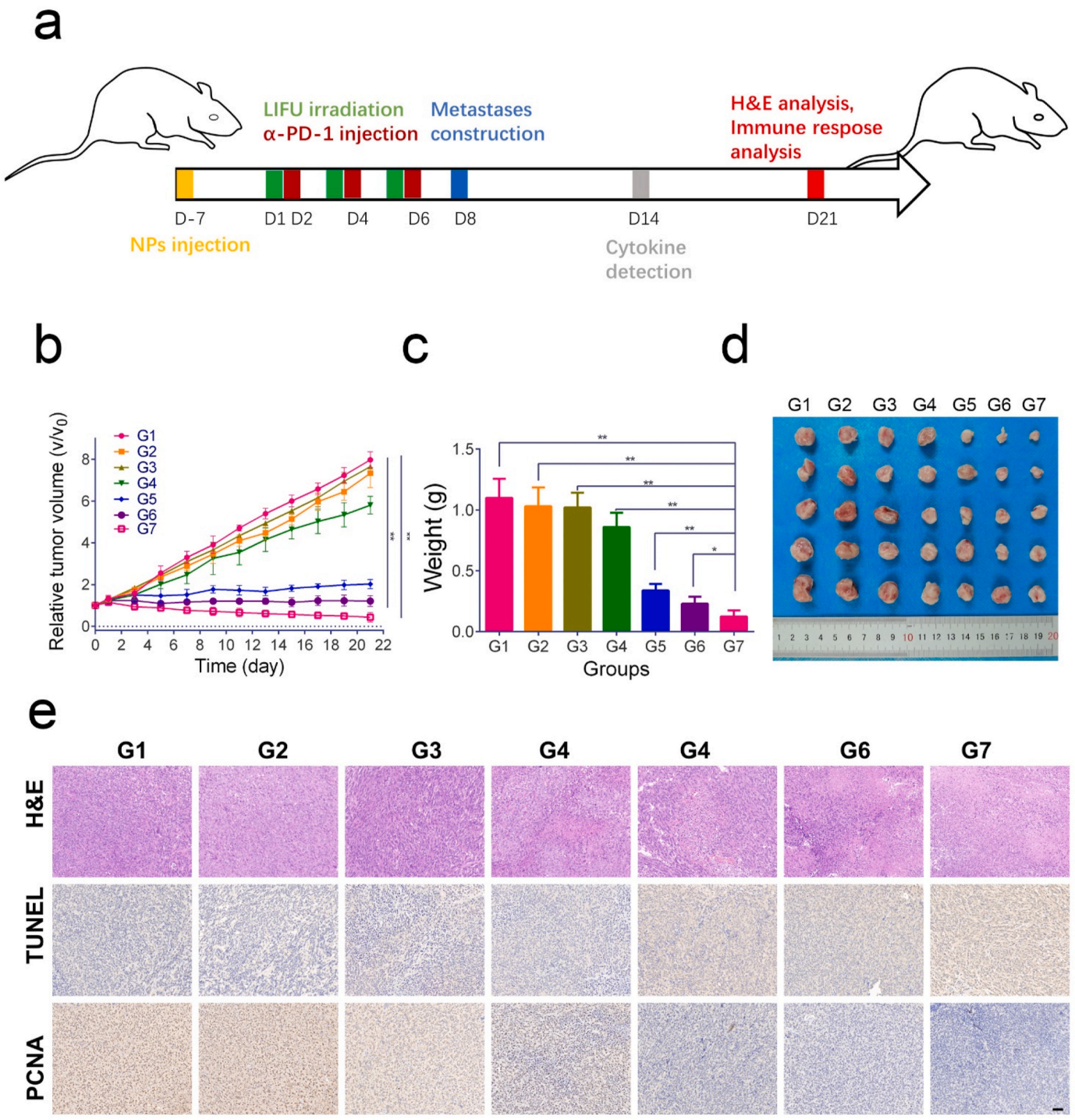

Fig. 5. (a) Schematic representation of the therapy schedule implemented in the 4T1 tumor model. (b) Tumor volume curves depicting the response to various treatments in mice (n = 5). (c) Tumor weights measured at the conclusion of treatment (n = 5). (d) Representative images showing excised tumors at the end of treatment following different interventions. (e) Histological analysis of tumor tissues through H&E, TUNEL, and PCNA staining across different treatment groups. Scale bar: 50 μm. (G1: Control, G2: LIFU, G3: PCCa, G4: PCCa + α-PD-1, G5: PCN + LIFU, G6: PCCa + LIFU, G7: PCCa + LIFU + α-PD-1), Statistical significance was assessed using one-way ANOVA. *$p < 0.05$, **$p < 0.01$.

(PCNA positive). Conversely, the PCCa + LIFU therapy group exhibited the least PCNA expression and the most significant necrosis in tumor tissues. These findings collectively suggested that combination therapy could effectively treat orthotopic breast cancers.

3.10. Anti-metastasis effects of PCCa

By conducting combination therapy, we observed that PCCa not only enhanced therapeutic efficacy but also prevented tumor metastasis by eliciting a robust immune response. Therefore, we evaluated the immunological response in mice. On day 8, 4T1 cells were intravenously injected into BALB/c mice bearing 4T1 tumors to establish a lung metastatic model. The first experiment assessed *in vivo* immune activation by measuring TNF-α and IFN-γ, two significant immune factors. Using ELISA, the levels of TNF-α and IFN-γ in serum were measured 13 days after the mice were first exposed to LIFU. As shown in Fig. 6a and b, the

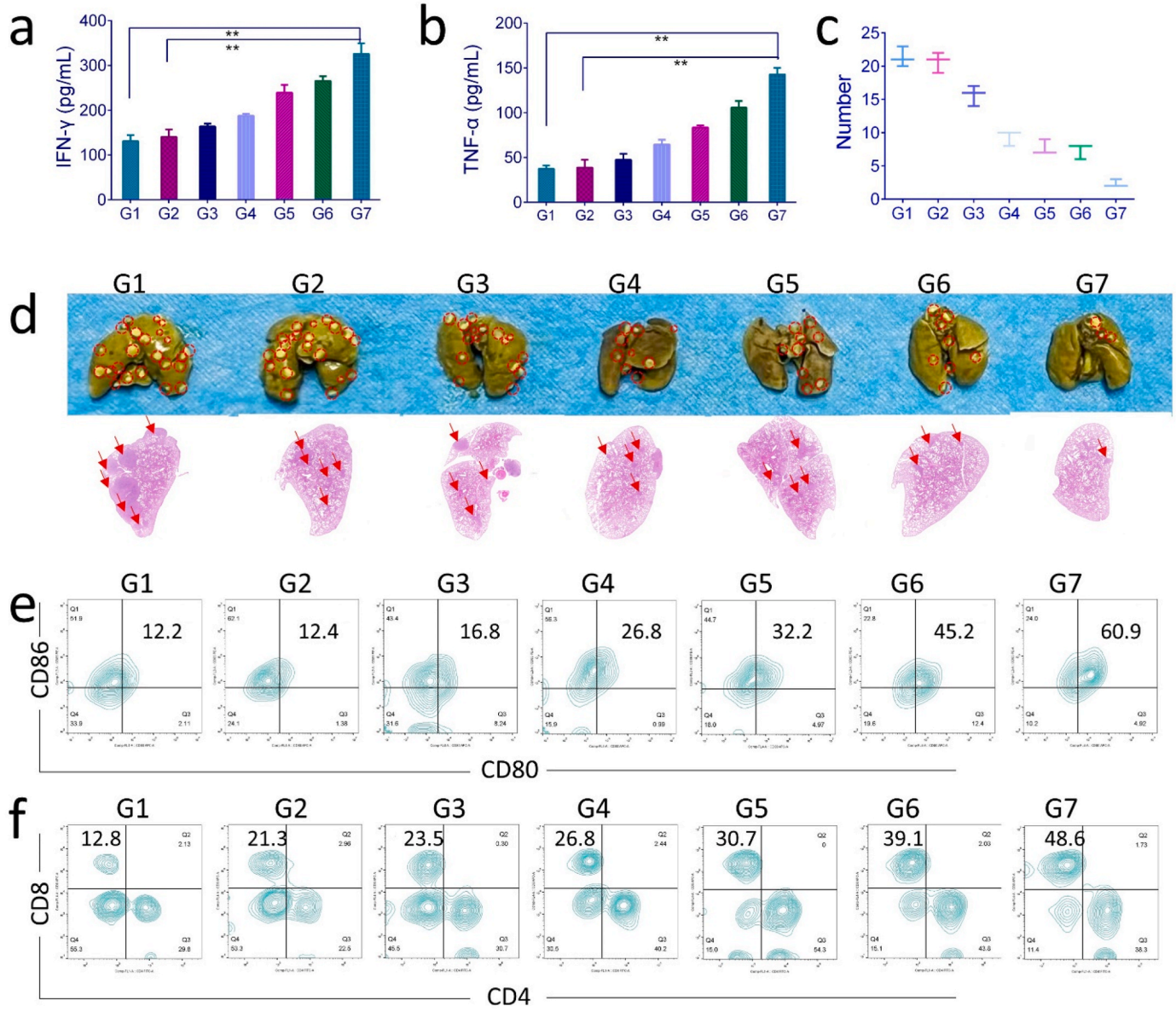

Fig. 6. Inhibiting effects of various treatments on the formation of lung metastatic tumors. The levels of (a) IFN-γ and (b) TNF-α in the tumor microenvironment at day 14 post-treatment with different formulations (n = 3). (c) Quantification of pulmonary metastatic nodules in mice treated with various formulations. (d) Representative photographs and corresponding H&E staining of metastatic foci in 4T1 lung metastatic tumors. Proportions of (e) mature DCs and (f) cytotoxic $CD8^+$ T cells in the tumor microenvironment at day 14 post-treatment with different formulations, assessed by flow cytometry. (G1: Control, G2: LIFU, G3: PCCa, G4: PCCa + α-PD-1, G5: PCN + LIFU, G6: PCCa + LIFU, G7: PCCa + LIFU + α-PD-1), Statistical significance was determined by one-way ANOVA. *$p < 0.05$, **$p < 0.01$.

combination of PCCa and α-PD-1 significantly increased IFN-γ and TNF-α levels, potentially activating the immune system through inflammatory pathways. To evaluate the effect of inhibiting lung metastatic tumor formation after PCCa injection during treatments, their lungs were isolated at the end of the experiment. The results showed obvious metastatic tumor nodules on the lung surface in the control group (Fig. 6c and d). The combined treatment group with PCCa plus α-PD-1 & LIFU showed fewer lung metastatic tumor lesions compared to other treated groups, which was further confirmed by H&E staining of lung tissues. These findings suggested that mice treated with PCCa + LIFU + α-PD-1 could inhibit the formation of metastatic foci in the lung. Taken together, these results could be attributed to the anticancer immune response activated by SDT and Ca^{2+} overload.

Immune responses at the tumor site were evaluated due to the immunogenic death and immunological activation induced by PCCa. DCs and $CD8^+$ T cell populations within the tumor microenvironment play essential roles in antigen presentation and cytotoxicity against tumor cells [45,46], and flow cytometry was performed to quantify their presence. As shown in Fig. 6e, the mature DC rate in the PCCa + LIFU + α-PD-1 group reached nearly 50 %. Compared with PCN + LIFU, PCCa + LIFU exhibited a significant immune activation effect. Additionally, as shown in Fig. 6f, mice in the PCCa + LIFU + α-PD-1 group exhibited the highest percentage of activated tumor-infiltrating $CD8^+$ T cells, indicating that PCCa can boost the immune response and prevent tumor metastasis when combined with therapeutic immune checkpoint inhibitors. These results indicate that PCCa-based SDT and Ca^{2+} overload therapy promote an anticancer immune response that can inhibit pulmonary metastasis.

4. Conclusion

In summary, we have developed a calcium ion nano-modulator

(PCCa) specifically designed for ROS-mediated calcium ion therapy. Upon internalization by cells, PCCa releases calcium ions and generates singlet oxygen upon ultrasonic irradiation. This production of reactive oxygen species disrupts cellular organelles and impairs the cell's ability to regulate calcium ions, thereby exacerbating the detrimental effects of calcium overload. Furthermore, under low-intensity focused ultrasound irradiation, the ROS-induced calcium overload triggers immunogenic cell death, leading to the activation of an antitumor immune response with PCCa acting as an adjuvant. Using a 4T1 tumor mouse model, PCCa exhibited remarkable efficacy in tumor eradication and significant anti-metastatic effects when combined with LIFU irradiation and immune checkpoint inhibitors, such as α-PD-1. This nanotherapeutic approach not only demonstrated substantial effectiveness against primary tumors but also displayed notable inhibitory effects on tumor metastasis. Overall, our findings highlight the potential of PCCa as a comprehensive and long-term strategy for improving antitumor treatment.

CRediT authorship contribution statement

Mi Yang: Writing – original draft, Methodology, Investigation, Formal analysis, Conceptualization. **Yaqin Hu:** Methodology, Formal analysis. **Xiuxiu Hao:** Methodology, Investigation. **Qiaoqi Chen:** Methodology, Formal analysis. **Yang Cao:** Supervision, Resources. **Haitao Ran:** Validation, Supervision, Methodology, Funding acquisition, Conceptualization. **Wei Zhang:** Writing – review & editing, Methodology, Funding acquisition, Formal analysis, Conceptualization.

Ethical approval statement

All animal experiments were approved by the Animal Ethics Committee of Chongqing Medical University.

Funding

This work was supported by the National Natural Science Foundation of China, China (82071926), the Science and Technology Research Program of Chongqing Municipal Education Commission, China (Grant No. KJZD-K202300403), Natural Science Foundation of Chongqing (CSTB2023NSCQ-MSX0149), and Joint Project of Pinnacle Disciplinary Group, the Second Affiliated Hospital of Chongqing Medical.

Declaration of competing interest

The authors declare that they have no known competing financial interests or personal relationships that could have appeared to influence the work reported in this paper.

Appendix A. Supplementary data

Supplementary data to this article can be found online at https://doi.org/10.1016/j.mtbio.2025.101666.

Data availability

Data will be made available on request.

References

[1] R.L. Siegel, K.D. Miller, N.S. Wagle, A. Jemal, Cancer statistics, CA Cancer J. Clin. 73 (1) (2023) 17–48, https://doi.org/10.3322/caac.21763, 2023.
[2] R. Hong, B. Xu, Breast cancer: an up-to-date review and future perspectives, Cancer Commun. 42 (10) (2022) 913–936, https://doi.org/10.1002/cac2.12358.
[3] N. Harbeck, M. Gnant, Breast cancer, Lancet 389 (10074) (2017) 1134–1150, https://doi.org/10.1016/s0140-6736(16)31891-8.
[4] M. Will, J. Liang, C. Metcalfe, S. Chandarlapaty, Therapeutic resistance to anti-oestrogen therapy in breast cancer, Nat. Rev. Cancer 23 (10) (2023) 673–685, https://doi.org/10.1038/s41568-023-00604-3.
[5] N. Mubtasim, N. Moustaid-Moussa, L. Gollahon, The complex biology of the obesity-induced, metastasis-promoting tumor microenvironment in breast cancer, Int. J. Mol. Sci. 23 (5) (2022), https://doi.org/10.3390/ijms23052480.
[6] R.U. Syed, M.D. Alshammari, H. Banu, W.M.A. Khojali, M. Jafar, P. Nagaraju, A. Alshammari, Targeting the autophagy-miRNA axis in prostate cancer: toward novel diagnostic and therapeutic strategies, N. Schmied. Arch. Pharmacol. (2024), https://doi.org/10.1007/s00210-024-03153-0.
[7] Y.C. Chae, J.H. Kim, Cancer stem cell metabolism: target for cancer therapy, BMB reports 51 (7) (2018) 319–326, https://doi.org/10.5483/bmbrep.2018.51.7.112.
[8] C. Cui, R. Merritt, L. Fu, Z. Pan, Targeting calcium signaling in cancer therapy, Acta Pharm. Sin. B 7 (1) (2017) 3–17, https://doi.org/10.1016/j.apsb.2016.11.001.
[9] S. Marchi, C. Giorgi, L. Galluzzi, P. Pinton, Ca(2+) fluxes and cancer, Mol Cell 78 (6) (2020) 1055–1069, https://doi.org/10.1016/j.molcel.2020.04.017.
[10] I. Rabinovich-Nikitin, L.A. Kirshenbaum, Circadian regulated control of myocardial ischemia-reperfusion injury, Trends Cardiovasc. Med. 34 (1) (2024) 1–7, https://doi.org/10.1016/j.tcm.2022.09.003.
[11] S. Romero-Garcia, H. Prado-Garcia, Mitochondrial calcium: transport and modulation of cellular processes in homeostasis and cancer, Int. J. Oncol. 54 (4) (2019) 1155–1167, https://doi.org/10.3892/ijo.2019.4696 (Review).
[12] A. Danese, S. Marchi, V.A.M. Vitto, L. Modesti, S. Leo, M.R. Wieckowski, C. Giorgi, P. Pinton, Cancer-related increases and decreases in calcium signaling at the endoplasmic reticulum-mitochondria interface (MAMs), reviews of physiology, biochemistry and pharmacology 185 (2023) 153–193, https://doi.org/10.1007/112_2020_43.
[13] N. Dhaouadi, V.A.M. Vitto, P. Pinton, L. Galluzzi, S. Marchi, Ca(2+) signaling and cell death, Cell Calcium 113 (2023) 102759, https://doi.org/10.1016/j.ceca.2023.102759.
[14] C. Huang, B. Lin, C. Chen, H. Wang, X. Lin, J. Liu, Q. Ren, J. Tao, P. Zhao, Y. Xu, Synergistic reinforcing of immunogenic cell death and transforming tumor-associated macrophages via a multifunctional cascade bioreactor for optimizing cancer immunotherapy, Adv Mater 34 (51) (2022) e2207593, https://doi.org/10.1002/adma.202207593.
[15] C. Wang, R. Zhang, X. Wei, M. Lv, Z. Jiang, Metalloimmunology: the metal ion-controlled immunity, Adv. Immunol. 145 (2020) 187–241, https://doi.org/10.1016/bs.ai.2019.11.007.
[16] Y. Yu, B.R. Xie, X.H. Liu, J.J. Ye, Z. Zhong, X.Z. Zhang, Mineralized porphyrin metal-organic framework for improved tumor elimination and combined immunotherapy, ACS Nano 17 (13) (2023) 12471–12482, https://doi.org/10.1021/acsnano.3c02126.
[17] Q. Li, Y. Chao, B. Liu, Z. Xiao, Z. Yang, Y. Wu, Z. Liu, Disulfiram loaded calcium phosphate nanoparticles for enhanced cancer immunotherapy, Biomaterials 291 (2022) 121880, https://doi.org/10.1016/j.biomaterials.2022.121880.
[18] X. Tan, J. Huang, Y. Wang, S. He, L. Jia, Y. Zhu, K. Pu, Y. Zhang, X. Yang, Transformable nanosensitizer with tumor microenvironment-activated sonodynamic process and calcium release for enhanced cancer immunotherapy, Angew Chem. Int. Ed. Engl. 60 (25) (2021) 14051–14059, https://doi.org/10.1002/anie.202102703.
[19] M.M. Al Omari, I.S. Rashid, N.A. Qinna, A.M. Jaber, A.A. Badwan, Calcium Carbonate, Profiles of Drug Substances, Excipients, and Related Methodology, vol. 41, 2016, pp. 31–132, https://doi.org/10.1016/bs.podrm.2015.11.003.
[20] A.S. Timin, A.S. Postovalova, T.E. Karpov, D. Antuganov, A.S. Bukreeva, D. R. Akhmetova, A.S. Rogova, A.R. Muslimov, S.A. Rodimova, D.S. Kuznetsova, M. V. Zyuzin, Calcium carbonate carriers for combined chemo- and radionuclide therapy of metastatic lung cancer, J Control Release 344 (2022) 1–11, https://doi.org/10.1016/j.jconrel.2022.02.021.
[21] K. Kahil, S. Weiner, L. Addadi, A. Gal, Ion pathways in biomineralization: perspectives on uptake, transport, and deposition of calcium, carbonate, and phosphate, J. Am. Chem. Soc. 143 (50) (2021) 21100–21112, https://doi.org/10.1021/jacs.1c09174.
[22] S.A. Shaked, S. Abehsera, A. Ziegler, S. Bentov, R. Manor, S. Weil, E. Ohana, J. Eichler, E.D. Aflalo, A. Sagi, A transporter that allows phosphate ions to control the polymorph of exoskeletal calcium carbonate biomineralization, Acta Biomater. 178 (2024) 221–232, https://doi.org/10.1016/j.actbio.2024.02.035.
[23] Y. Zhou, J. Jiao, R. Yang, B. Wen, Q. Wu, L. Xu, X. Tong, H. Yan, Temozolomide-based sonodynamic therapy induces immunogenic cell death in glioma, Clin Immunol 256 (2023) 109772, https://doi.org/10.1016/j.clim.2023.109772.
[24] T.G. Nguyen Cao, Q. Truong Hoang, J.H. Kang, S.J. Kang, V. Ravichandran, W. J. Rhee, M. Lee, Y.T. Ko, M.S. Shim, Bioreducible exosomes encapsulating glycolysis inhibitors potentiate mitochondria-targeted sonodynamic cancer therapy via cancer-targeted drug release and cellular energy depletion, Biomaterials 301 (2023) 122242, https://doi.org/10.1016/j.biomaterials.2023.122242.
[25] Z. Chen, W. Liu, Z. Yang, Y. Luo, C. Qiao, A. Xie, Q. Jia, P. Yang, Z. Wang, R. Zhang, Sonodynamic-immunomodulatory nanostimulators activate pyroptosis and remodel tumor microenvironment for enhanced tumor immunotherapy, Theranostics 13 (5) (2023) 1571–1583, https://doi.org/10.7150/thno.79945.
[26] J. Huang, D. Liao, Y. Han, Y. Chen, S. Raza, C. Lu, J. Liu, Q. Lan, Current status of porous coordination networks (PCNs) derived porphyrin spacers for cancer therapy, Expet Opin. Drug Deliv. 20 (9) (2023) 1209–1229, https://doi.org/10.1080/17425247.2023.2260309.
[27] A. Som, R. Raliya, L. Tian, W. Akers, J.E. Ippolito, S. Singamaneni, P. Biswas, S. Achilefu, Monodispersed calcium carbonate nanoparticles modulate local pH and inhibit tumor growth in vivo, Nanoscale 8 (25) (2016) 12639–12647, https://doi.org/10.1039/c5nr06162h.
[28] Y. Bao, J. Chen, H. Qiu, C. Zhang, P. Huang, Z. Mao, W. Tong, Erythrocyte membrane-camouflaged PCN-224 nanocarriers integrated with platinum

nanoparticles and glucose oxidase for enhanced tumor sonodynamic therapy and synergistic starvation therapy, ACS applied materials & interfaces 13 (21) (2021) 24532–24542, https://doi.org/10.1021/acsami.1c05644.
[29] F. Hao, Z.Y. Yan, X.P. Yan, Intracellular fate and immune response of porphyrin-based nano-sized metal-organic frameworks, Chemosphere 307 (Pt 2) (2022) 135680, https://doi.org/10.1016/j.chemosphere.2022.135680.
[30] W. Zhang, C. Zhang, C. Yang, X. Wang, W. Liu, M. Yang, Y. Cao, H. Ran, Photochemically-driven highly efficient intracellular delivery and light/hypoxia programmable triggered cancer photo-chemotherapy, J Nanobiotechnology 21 (1) (2023) 11, https://doi.org/10.1186/s12951-023-01774-w.
[31] H. Yuan, K. Chen, J. Geng, Z. Wu, C. Wang, P. Shi, Metal-organic framework PCN-224 combined cobalt oxide nanoparticles for hypoxia relief and synergistic photodynamic/chemodynamic therapy, Chemistry (2024) e202400319, https://doi.org/10.1002/chem.202400319.
[32] Y. Zeng, Q. Ouyang, Y. Yu, L. Tan, X. Liu, Y. Zheng, S. Wu, Defective homojunction porphyrin-based metal-organic frameworks for highly efficient sonodynamic therapy, Small Methods 7 (1) (2023) e2201248, https://doi.org/10.1002/smtd.202201248.
[33] J. Huang, J. He, J. Wang, Y. Li, Z. Xu, L. Zhang, Y. Kang, P. Xue, Calcium carbonate-actuated ion homeostasis perturbator for oxidative damage-augmented Ca(2+)/Mg(2+) interference therapy, Biomaterials 302 (2023) 122340, https://doi.org/10.1016/j.biomaterials.2023.122340.
[34] I. Canton, G. Battaglia, Endocytosis at the nanoscale, Chem. Soc. Rev. 41 (7) (2012) 2718–2739, https://doi.org/10.1039/c2cs15309b.
[35] C. Wang, T. Li, Z. Wang, Y. Li, Y. Liu, M. Xu, Z. Zhang, Y. Deng, L. Cai, C. Zhang, C. Li, Nano-modulators with the function of disrupting mitochondrial Ca(2+) homeostasis and photothermal conversion for synergistic breast cancer therapy, J Nanobiotechnology 21 (1) (2023) 465, https://doi.org/10.1186/s12951-023-02220-7.
[36] N. Alrushaid, F.A. Khan, E.A. Al-Suhaimi, A. Elaissari, Nanotechnology in cancer diagnosis and treatment, Pharmaceutics 15 (3) (2023), https://doi.org/10.3390/pharmaceutics15031025.
[37] X. Dong, C. Zang, Y. Sun, S. Zhang, C. Liu, J. Qian, Hydroxyapatite nanoparticles induced calcium overload-initiated cancer cell-specific apoptosis through inhibition of PMCA and activation of calpain, J. Mater. Chem. B 11 (32) (2023) 7609–7622, https://doi.org/10.1039/d3tb00542a.
[38] D. Wu, Z.Q. Zhu, H.X. Tang, Z.E. Shi, J. Kang, Q. Liu, J. Qi, Efficacy-shaping nanomedicine by loading calcium peroxide into tumor microenvironment-responsive nanoparticles for the antitumor therapy of prostate cancer, Theranostics 10 (21) (2020) 9808–9829, https://doi.org/10.7150/thno.43631.
[39] H. Kim, D.G. Lee, Naringin-generated ROS promotes mitochondria-mediated apoptosis in Candida albicans, IUBMB Life 73 (7) (2021) 953–967, https://doi.org/10.1002/iub.2476.
[40] Y. Gong, S. Luo, P. Fan, H. Zhu, Y. Li, W. Huang, Growth hormone activates PI3K/Akt signaling and inhibits ROS accumulation and apoptosis in granulosa cells of patients with polycystic ovary syndrome, Reprod. Biol. Endocrinol. : RB&E 18 (1) (2020) 121, https://doi.org/10.1186/s12958-020-00677-x.
[41] D. Tang, R. Kang, C.B. Coyne, H.J. Zeh, M.T. Lotze, PAMPs and DAMPs: signal 0s that spur autophagy and immunity, Immunol. Rev. 249 (1) (2012) 158–175, https://doi.org/10.1111/j.1600-065X.2012.01146.x.
[42] F. Kianian, M. Kadkhodaee, H.R. Sadeghipour, S.M. Karimian, B. Seifi, An overview of high-mobility group box 1, a potent pro-inflammatory cytokine in asthma, J. Basic Clin. Physiol. Pharmacol. 31 (6) (2020), https://doi.org/10.1515/jbcpp-2019-0363.
[43] H. Jin, Y.S. Ko, H.J. Kim, P2Y2R-mediated inflammasome activation is involved in tumor progression in breast cancer cells and in radiotherapy-resistant breast cancer, Int. J. Oncol. 53 (5) (2018) 1953–1966, https://doi.org/10.3892/ijo.2018.4552.
[44] H. Desikan, A. Kaur, I.D. Pogozheva, M. Raghavan, Effects of calreticulin mutations on cell transformation and immunity, J. Cell Mol. Med. 27 (8) (2023) 1032–1044, https://doi.org/10.1111/jcmm.17713.
[45] Q. Chen, L. Xu, C. Liang, C. Wang, R. Peng, Z. Liu, Photothermal therapy with immune-adjuvant nanoparticles together with checkpoint blockade for effective cancer immunotherapy, Nat. Commun. 7 (2016) 13193, https://doi.org/10.1038/ncomms13193.
[46] H. Phuengkham, C. Song, Y.T. Lim, A designer scaffold with immune nanoconverters for reverting immunosuppression and enhancing immune checkpoint blockade therapy, Adv Mater 31 (42) (2019) e1903242, https://doi.org/10.1002/adma.201903242.